Chapter 4
Practical Aspects of Kelvin Probe Force Microscopy in Liquids

Kei Kobayashi and Hirofumi Yamada

Abstract There has been a strong demand for the development of scanning probe techniques that can map the distribution of surface charge and surface potential at nanometer scale in liquid media. While electrostatic force microscopy (EFM) and Kelvin probe force microscopy (KPFM) have routinely been used in vacuum and ambient conditions, they are not readily applicable in polar liquid media. In this chapter, we review the practical aspects of electrostatic and capacitive force detection in liquids and discuss the feasibility of measuring the surface charge or potential distribution in polar liquid media.

4.1 Introduction

Electrostatic force microscopy (EFM) and Kelvin probe force microscopy (KPFM) are scanning probe techniques for mapping local surface charge and potential. These methods utilize the detection of the electrostatic forces induced by an alternating modulation voltage that is applied between the tip and sample surface. These methods have been commonly used under ambient conditions as well as in vacuum environments. Recently, there has been a strong demand for local surface charge and potential measurements in polar liquids, especially in aqueous solutions containing electrolytes (ions). However, since the surface charges are screened by the surrounding counter ions in aqueous solutions, forming an electric double layer (EDL), the electrostatic interaction between tip and surface is not as simple as that in vacuum or air.

The spatial resolution of the scanning probe techniques stems from the strong distance dependence of the tip-sample interaction. We first review the potential profile of the EDL and analyze the electrostatic force as well as the capacitive force acting between the tip and sample in terms of the tip-sample distance dependence, that is critical for obtaining high spatial resolution in the local surface charge and

K. Kobayashi (✉) · H. Yamada
Kyoto University, Kyoto, Japan
e-mail: keicoba@iic.kyoto-u.ac.jp

S. Sadewasser and T. Glatzel (eds.), *Kelvin Probe Force Microscopy*,
Springer Series in Surface Sciences 65, https://doi.org/10.1007/978-3-319-75687-5_4

potential measurements. We then discuss the possibility of the local surface charge and potential measurements in liquid media using voltage modulation techniques in detail and present some criteria for achieving nanometer-scale surface charge and potential measurements. Finally, we also demonstrate the surface charge measurement on a biological sample using the three-dimensional (3D) force mapping technique, as an alternative method to map the local surface charge and potential in liquid media.

4.2 Electric Double Layer

In this section, we review the basic properties of the EDL [1]. When a charged surface is exposed to an aqueous solution containing ions, counter ions having the charge opposite to the surface charge in the solution are attracted to the charged surface, which causes a density gradient toward the charged surface. The distribution of the ion of any species i in the solution follows the Boltzmann distribution, given by

$$n_i = n_i^{\infty} \exp\left(- \frac{z_i e \phi}{k_B T} \right), \tag{4.1}$$

where ϕ is the potential measured with respect to the bulk solution, e and z_i are the elementary charge and the ion valence, n_i^{∞} is the ion concentration in the bulk solution, and k_B and T are the Boltzmann constant and temperature. The total charge density is thus given by

$$\rho = \sum_i z_i e n_i = e \sum_i z_i n_i. \tag{4.2}$$

Since the charge density is related to the potential by the Poisson's equation as

$$\rho = - \varepsilon_r \varepsilon_0 \nabla^2 \phi, \tag{4.3}$$

we obtain the Poisson-Boltzmann equation by combining (4.1) and (4.3), which is given by

$$\nabla^2 \phi = - \frac{e}{\varepsilon_r \varepsilon_0} \sum_i z_i n_i^{\infty} \exp\left(- \frac{z_i e \phi}{k_B T} \right). \tag{4.4}$$

Here we consider the one-dimensional (1D) capacitor model, in which a pair of planar metallic electrodes are facing each other in an aqueous solution, as shown in Fig. 4.1a. The Poisson-Boltzmann equation for the 1D capacitor model is given by

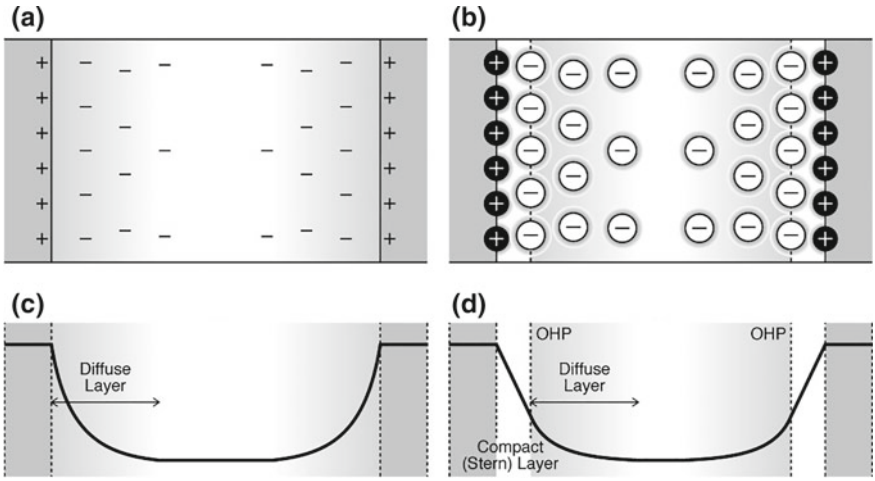

Fig. 4.1 Schematic model of equally charged electrodes in electrolyte. **a** Gouy-Chapman model. **b** Potential profile in Gouy-Chapman model. **c** Gouy-Chapman-Stern (GCS) model. **d** Potential profile in GCS model. OHP stands for the outer Helmholtz plane, which is defined as the surface of the compact layer

$$\frac{\mathrm{d}^2}{\mathrm{d}x^2}\phi(x) = -\frac{e}{\varepsilon_\mathrm{r}\varepsilon_0}\sum_i z_i n_i^\infty \exp\left(-\frac{z_i e\,\phi}{k_\mathrm{B}T}\right), \tag{4.5}$$

where x is a coordinate. In order to further simplify the equation, we consider the case where only monovalent ions exist in the solution (a 1:1 electrolyte). In this case, the equation is simplified as

$$\frac{\mathrm{d}^2}{\mathrm{d}x^2}\phi(x) = \frac{en^\infty}{\varepsilon_\mathrm{r}\varepsilon_0}\sinh\left(\frac{e\phi}{k_\mathrm{B}T}\right), \tag{4.6}$$

where n^∞ is the concentration of the monovalent ions. By solving (4.6) with a boundary condition of the surface potential at the charged surface, $\phi(0) = \phi_\mathrm{D}$, we obtain

$$\frac{\tanh[e\phi/(4k_\mathrm{B}T)]}{\tanh[e\phi_\mathrm{D}/(4k_\mathrm{B}T)]} = e^{-\kappa_\mathrm{D}x}, \tag{4.7}$$

where κ_D is given by

$$\kappa_\mathrm{D} = \sqrt{\frac{2\,e^2 n^\infty}{\varepsilon_\mathrm{r}\varepsilon_0 k_\mathrm{B}T}}. \tag{4.8}$$

κ_D^{-1} is the so-called the Debye screening length (L_D) corresponding to the thickness of the diffuse layer, in which the concentration of the counter ions is higher than in the bulk. Figure 4.1b shows a potential profile of a pair of equally charged electrodes. The left-hand side of (4.7) can be simplified as

$$\frac{\phi(x)}{\phi_D} = \exp(-\kappa_D x), \tag{4.9}$$

when the surface potential is low and the condition

$$e\phi_D/(4\,k_B T) < 0.5, \tag{4.10}$$

is met, namely for $\phi_D < 50\,\mathrm{mV}$. Note that (4.9) is the solution of the linearized version of the 1D Poisson-Boltzmann equation, which is given by

$$\frac{d^2\phi(x)}{dx^2} = \kappa_D^2 \phi(x). \tag{4.11}$$

Since the relationship between the surface potential and the surface charge density is determined by Gauss's law, the surface charge on the electrode with the potential ϕ_D is given by

$$\sigma_s = -\varepsilon_r \varepsilon_0 \left.\frac{d\phi(x)}{dx}\right|_{x=0} = \sqrt{8k_B T \varepsilon_r \varepsilon_0 n^\infty}\,\sinh\left(\frac{e\phi_D}{2k_B T}\right), \tag{4.12}$$

and the capacitance of the diffuse layer per unit area is defined by

$$C_D = \frac{d\sigma_s}{d\phi_D} = \sqrt{\frac{2e^2 \varepsilon_r \varepsilon_0 n^\infty}{k_B T}}\cosh\left(\frac{e\phi_D}{2k_B T}\right) = \kappa_D \varepsilon_r \varepsilon_0 \cosh\left(\frac{e\phi_D}{2k_B T}\right). \tag{4.13}$$

This simple interface model is referred to as the Gouy-Chapman model. Since the model fails to explain the experimentally measured capacitance versus voltage characteristics, Stern modified the Gouy-Chapman model by taking into account the finite size of the ions and introduced an idea of a thin layer (compact layer or Stern layer) on the surface where even the bound counter ions cannot reach, as shown schematically in Fig. 4.1c. Since the charge density in the compact layer is zero, the capacitance of the compact layer per unit area is simply given by

$$C_S = \frac{\varepsilon_r \varepsilon_0}{t_c}, \tag{4.14}$$

where t_c is the thickness of the compact layer. Now the surface potential of the electrode is modified to

$$\phi_0 = \phi_D + \sqrt{\frac{8k_B T n^\infty}{\varepsilon_r \varepsilon_0}} \sinh\left(\frac{e\phi_D}{2k_B T}\right) t_c. \tag{4.15}$$

This interface model is referred to as the Gouy-Chapman-Stern (GCS) model, in which the EDL is composed of two layers; i.e., the diffuse layer and the compact layer. Figure 4.1d shows a potential profile of a pair of equally charged electrodes in the GCS model.

4.3 Capacitive Force

The electrostatic force acting between tip and sample in EFM or KPFM (F_{el}) is generally described as

$$F_{el} = \frac{1}{2}\frac{dC_{ts}}{dz} V_{ts}^2, \tag{4.16}$$

where C_{ts} is the capacitance between tip and sample, V_{ts} is the voltage between tip and sample, and z is the tip-sample distance. When a modulation voltage of an amplitude V_{ac} at an angular frequency ω_m (frequency: f_m) with a dc offset voltage V_{dc}, namely $V_m = V_{dc} + V_{ac}\cos(\omega_m t)$, is applied between tip and sample, the electrostatic force becomes

$$F_{el} = \frac{1}{2}\frac{dC_{ts}}{dz}\left[(V_{dc} + V_{SP})^2 + \frac{1}{2}V_{ac}^2 + 2(V_{dc} + V_{SP})V_{ac}\cos(\omega_m t) + \frac{1}{2}V_{ac}^2\cos(2\,\omega_m t)\right] \tag{4.17}$$

where V_{SP} is the surface potential difference between tip and sample. The last term in the equation ($2\omega_m$ component) is often referred to as the capacitive force.

In order to analyze the electrostatic force acting between tip and sample that is induced by the modulation voltage, it is important to understand the voltage drop of the modulation voltage between a pair of electrodes which are facing each other [2]. The equivalent circuit for a pair of facing electrodes in electrolyte can be depicted as shown in Fig. 4.2a. Note that the circuit is valid only when the EDLs of the surfaces do not overlap with each other. In this model, the EDL capacitance C_{EDL} is comprised of a series of the compact (Stern) layer capacitance C_S and the diffuse layer capacitance C_D. The impedance of the bulk solution is expressed by a parallel circuit of the bulk solution resistance per unit area, R_B, and capacitance per unit area, C_B. R_B is described as

$$R_B = d\rho_B, \tag{4.18}$$

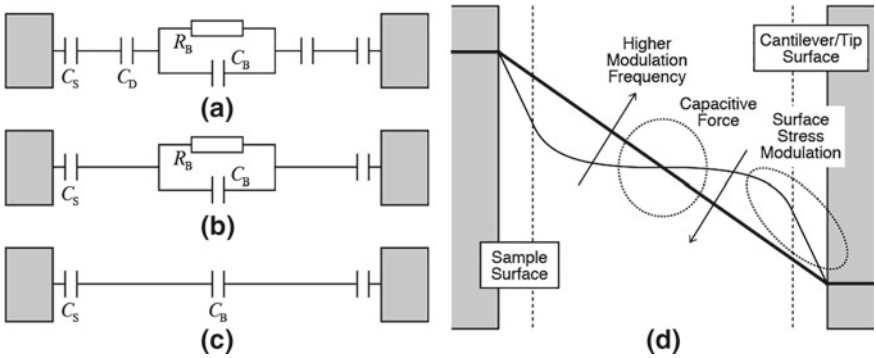

Fig. 4.2 Equivalent circuits for a pair of facing electrodes in aqueous solutions for a modulation frequency (f_m) in the ranges of **a** $f_m < f_D$, **b** $f_D < f_m < f_c$, and **c** $f_c < f_m$. **d** Snapshot of the potential profile when the voltage of the sample is positive with respect to the cantilever and tip. In the low modulation frequency regime ($f_m < f_D$), only the potential gradient (electric field) at the interface is modulated, and the cantilever deflection is predominantly caused by the surface stress variation. In the high modulation frequency regime ($f_c < f_m$), the electric field in the bulk solution is effectively modulated, and the cantilever deflection is predominantly caused by the capacitive force

where d and ρ_B are the distance between the electrodes and the resistivity of the electrolyte, respectively.

When f_m is very low, the modulation voltage is effectively applied to the electrode/electrolyte interface, and charge and discharge of the diffuse layer occur with an ionic current flow in the bulk solution. This happens when f_m is lower than a threshold frequency (f_D), which is defined as the frequency at which the impedance of C_D becomes smaller than R_B, i.e.,

$$f_D = \frac{1}{2\pi R_B (C_D/2)} = \frac{1}{\pi d \kappa_D \varepsilon_r \varepsilon_0 \rho_B \cosh\left(\frac{eV_{ac}^D}{2k_B T}\right)} \propto \frac{\sqrt{n^\infty}}{\varepsilon_r}, \tag{4.19}$$

where V_{ac}^D is the magnitude of the modulation voltage applied to the diffuse layer, which roughly corresponds to $V_{ac}/2$ because V_{ac} is effectively applied to the two diffuse layers and divided by the two. In this case, the impedance of the bulk solution is dominated by the bulk solution resistance R_B, and most of the modulation voltage is effectively applied to C_D, which does not depend on the tip-sample distance. This causes a modulation in the cantilever deflection induced by the surface stress variation [3, 4]. Therefore, f_m should be higher than f_D for EFM or KPFM in aqueous solutions.

Even though this criterion is met; i.e. f_m is higher than f_D, ionic current flow still occurs in the bulk solution; the equivalent circuit in this regime is depicted in Fig. 4.2b. Therefore, f_m should be even higher than another threshold frequency, namely the characteristic relaxation frequency of the ionic current flow (f_c), which is dependent only on the physical property of the solution, defined as

$$f_c = \frac{1}{2\pi\varepsilon_r\varepsilon_0\rho_B} \propto \frac{n_\infty}{\varepsilon_r}. \tag{4.20}$$

If this criterion is met, the impedance of C_B becomes smaller than R_B, and thus a further simplified equivalent circuit, shown in Fig. 4.2c, can be used.

Figure 4.2d illustrates a potential profile between tip and sample for an alternating modulation voltage [2, 5]. The figure depicts a snapshot of the potential profile when the voltage of the sample is positive with respect to the cantilever with a tip. The thin voltage potential curve corresponds to the profile for a lower modulation frequency ($f_m < f_D$: Fig. 4.2a), while the thick voltage potential curve corresponds to that for a higher modulation frequency ($f_m > f_c$: Fig. 4.2c). In the former case the cantilever deflection induced by the surface stress variation is prominent, while in the latter case the modulation voltage is effectively applied in C_B and the cantilever deflection induced by the capacitive force is expected.

We can calculate the capacitive force in aqueous solutions as a function of the tip-sample distance. The total capacitive force acting on a cantilever with a tip is considered as a sum of the force components acting on a spherical tip apex, a conical tip body, and a cantilever part [6, 7]. Each component can be calculated by integrating the force acting on a unit area by taking the voltage division ratio between C_B and C_S into account for each component [2]. It should be noted that the capacitive force as well as the electrostatic force at the tip-sample distance of less than a few tens of nanometers is affected by the dielectric saturation, i.e. the reduction of the dielectric constant in the EDL in the case of a high electric field [8, 9]. The Booth equation is generally used for the dielectric saturation, which is given by

$$\varepsilon_r(E) = n_w^2 + \frac{3\left(\varepsilon_r^\infty - n_w^2\right)}{\beta E}\left[\coth(\beta E) - \frac{1}{\beta E}\right], \tag{4.21}$$

where n_w is the refractive index of water, and β is given by

$$\beta = \frac{5\mu_w\left(n_w^2 + 2\right)}{2k_B T}, \tag{4.22}$$

where μ_w is the electric dipole moment of a water molecule. Although the dielectric constant is a nonlinear function of the electric field, it can be approximated to a parabolic form when the electric field is less than 0.1 V/nm as

$$\varepsilon_r(E) \approx \varepsilon_r^\infty - \nu E^2, \tag{4.23}$$

using a constant ν.

4.4 Electrostatic Force

Here, we consider the variation in the potential profile when the tip-sample distance is reduced. Figure 4.3a shows a schematic of ac potential profiles for a large and a short distance with f_m higher than f_c. As the tip-sample distance decreases, the alternating electric field in the bulk solution is increased. However, because of the increase in C_B, the voltage division ratio between C_B and C_S also changes. In other words, the potential drop in C_S also increases by the reduction of the tip-sample distance. This phenomenon deteriorates the spatial resolution of the electrostatic force as well as the capacitive force measurements [2].

We also calculated the electric field induced by an externally applied dc voltage (V_{dc}), as shown in Fig. 4.3b. In the GCS model, when the distance between the electrodes is large and there is no overlap of the EDLs ($d > 2L_D$), the potential gradient at the midpoint is almost zero. As the two surfaces come close to each other, an increase in the potential gradient at the midpoint is expected due to the charge regulation [10, 11].

We can calculate the electrostatic force per unit area, namely the Maxwell stress (T_{el}) using the dc electric field $\left(E_{dc}^{m}\right)$ and ac electric field $\left(E_{dc}^{m}\right)$ at the midpoint ($x = d/2$) as

$$T_{el}(\omega_m) = \frac{1}{2}\varepsilon_r\varepsilon_0 E^2 = \frac{1}{2}\varepsilon_r\varepsilon_0\left[E_{dc}^{m} + E_{ac}^{m}\cos(\omega_m t)\right]^2$$
$$= \frac{1}{2}\varepsilon_0\varepsilon_r\left[\left(E_{dc}^{m}\right)^2 + \frac{1}{2}\left(E_{ac}^{m}\right)^2 + 2E_{dc}^{m}E_{ac}^{m}\cos(\omega_m t) + \frac{1}{2}\left(E_{ac}^{m}\right)^2\cos(2\omega_m t)\right]. \tag{4.24}$$

The dc electric field at the midpoint can be calculated from the dc potential profile between the electrodes. The potential of the electrode surface can be

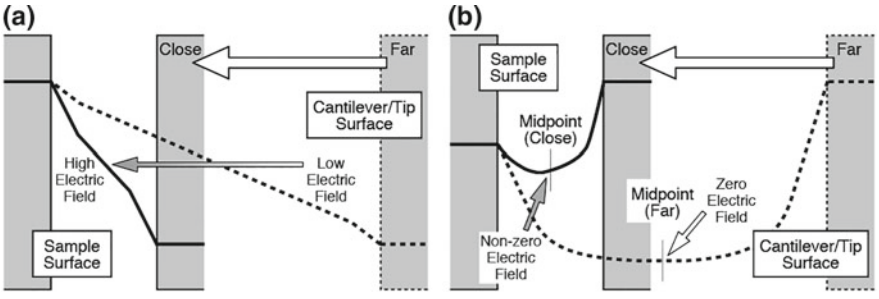

Fig. 4.3 **a** Schematic of ac potential profiles between a pair of facing electrodes in aqueous solution for two tip-sample distances. The ac potential profiles depict an instantaneous maximum voltage for the case when V_{ac} is applied to the left electrode (sample) with respect to the right electrode (cantilever with a tip). **b** Schematic of dc potential profiles between a pair of facing electrodes for two tip-sample distances

considered as constant in weak electrolyte solutions such as pure water [11]. For the calculation of the dc potential profile between the two electrodes, an analytical solution expressing the relationship of d, ϕ_0, and E is required. However, the analytical solution of the Poisson-Boltzmann equation can be obtained only in the case when ϕ_d is less than 50 mV and the distance between the surfaces is larger than L_D [12]. Therefore, we used an approximate equation, which is valid for arbitrary potential, by the linear superposition approximation (LSA) [13]. The dc electric field at the midpoint between the surfaces is expressed as

$$E_{dc}^{m} = -\left.\frac{d\phi_{dc}}{dx}\right|_{x=d/2} = \frac{2k_BT}{de}\left\{-\ln\left[\frac{1+\gamma_1 e^{-\frac{\kappa_D d}{2}}}{1-\gamma_1 e^{-\frac{\kappa_D d}{2}}}\right] + \ln\left[\frac{1+\gamma_2 e^{-\frac{\kappa_D d}{2}}}{1-\gamma_2 e^{-\frac{\kappa_D d}{2}}}\right]\right\} + \frac{4\kappa_D k_B T}{de}(-\gamma_1+\gamma_2)e^{-\frac{\kappa_D d}{2}}, \tag{4.25}$$

where γ_i is given by

$$\gamma_i = \tanh\left(\frac{e\phi_i}{4k_BT}\right). \tag{4.26}$$

The first and second terms in (4.25) are the dc electric field at the midpoint when the EDLs of the surfaces are not overlapping, and that when they are overlapping, respectively. On the other hand, the ac electric field at the midpoint between the surfaces is expressed as

$$E_{ac}^{m} = -\left.\frac{d\phi_{ac}}{dx}\right|_{x=d/2} = \frac{V_{ac}}{d}\frac{1+2\frac{C_B}{C_S}}{\left(2\frac{C_B}{C_S}\frac{f_c}{f_m}\right)^2 + \left(1+2\frac{C_B}{C_S}\right)^2}\cos(\omega_m t) \tag{4.27}$$

taking the voltage division ratio into account. Furthermore, we took into account the dielectric saturation [8, 9].

We measured the electrostatic and capacitive forces induced on a conductive cantilever with a tip when an alternating voltage is applied between the cantilever and a sample surface in aqueous solutions [14]. We found that the electrostatic force contribution to the cantilever deflection becomes dominant when a high modulation frequency was used. However, we could not observe the steep increase in the electrostatic force that should be expected for the electrostatic force acting on the tip apex. On the contrary, we observed the electrostatic force even when the cantilever was far from the sample surface, despite that the potential gradient at the midpoint is expected to be almost zero in the GCS model (see Fig. 4.3b) and thereby negligible electrostatic force since there is no overlap of the EDLs ($d > 2L_D$). We consider that this is due to the alternating electric field being directly applied to C_B between the cantilever part and sample surface with a high modulation frequency

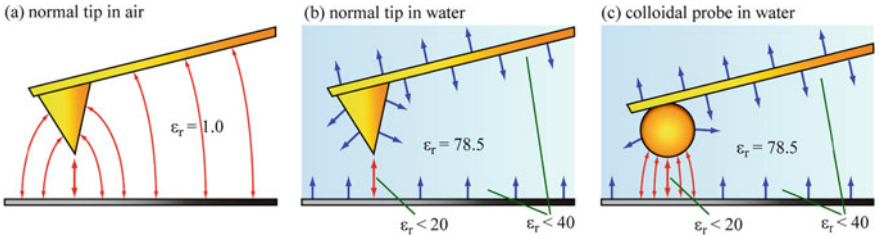

Fig. 4.4 Schematics of the electric field distributions in the experimental conditions with a metal-coated regular cantilever with a tip in **a** air, **b** water, and **c** a metal-coated colloidal probe (CP) cantilever in water. The red arrows show the electric field between the tip and the sample, and the blue arrows show the electric field in the EDLs. Reprinted from J. Appl. Phys. 116, 134307 (2014) with the permission of AIP Publishing

(large E_{ac}^{m}) and thus an unexpected voltage drop in the bulk solution (nonzero E_{dc}^{m}) could cause a significant electrostatic force on the cantilever part since it is proportional to the product of E_{ac}^{m} and E_{dc}^{m}. Therefore, we consider that we need to reduce the long-range parasitic electrostatic force acting on the cantilever.

We measured the capacitive and electrostatic force in an aqueous solution using a colloidal probe (CP) cantilever to demonstrate the effect of the reduction of the long-range parasitic electrostatic force. Figure 4.4a shows the schematics of the dc electric field distribution between a cantilever with a regular sharp tip and the sample in air. The electric field exists between the entire cantilever and the sample. On the other hand, Fig. 4.4b shows the dc electric field distribution between a regular cantilever and a sample in water. Since the dc electric field is screened by the EDLs, there should be no dc electric field at the midpoint between the cantilever part and sample. However, we indeed observed the long-range parasitic electrostatic force acting on the cantilever part. Figure 4.4c shows the dc electric field distribution between a CP cantilever and a sample in water. Since the effective interaction area of the CP is much larger than that of the regular cantilever, it is expected that we could detect the electrostatic force acting on the CP that overwhelms the parasitic electrostatic force acting on the cantilever part by using the CP cantilever.

We used the second resonance mode of the CP cantilever, which was around 855 kHz, in order to excite the cantilever at a high frequency. The spring constant and quality factor at the second resonance were determined as 1,350 N/m and 12, respectively. Figure 4.5a shows the amplitude of the ω_m component as a function of V_{dc} obtained when the tip-sample distance was kept at about 10 nm in pure water. V_{dc} and V_{ac} were set at 0 V and 2.8 V peak-to-peak, respectively. The result shows that the hysteresis caused by the surface stress effect is negligible, but no minimum point was observed in this measurement range. This fact means that the KPFM bias voltage feedback cannot be used even using the CP cantilever. As explained in Fig. 4.3b, V_{dc} mainly drops at C_S, while the electric field in C_B matters the measured electrostatic force. Depending on the combination of the materials of tip and sample and the electrolyte, the force minimum might be observed in the

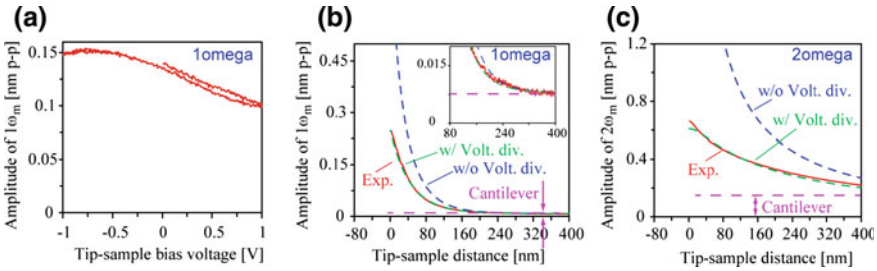

Fig. 4.5 **a** Amplitude of ω_m as a function of V_{dc} in water. Amplitudes of **b** ω_m component ($f_m = f_2 = 855$ kHz) and **c** $2\omega_m$ component ($f_m = f_2/2 = 378$ kHz) of the cantilever deflection signal as a function of the tip-sample distance in water. The inset in **b** shows the magnified data at large distance. The red, blue, and green curves show the experimental curve, theoretically fitted curve without taking into account the voltage division ratio, and with it, respectively. The purple broken line shows the offset in the oscillation amplitude caused by the electrostatic/capacitive force acting on the cantilever other than the colloid. Reprinted from J. Appl. Phys. 116, 134307 (2014) with the permission of AIP Publishing

measurement range, but it is difficult to estimate the surface potential difference anyway.

Figure 4.5b, c show plots of the amplitudes of the ω_m and $2\omega_m$ components as a function of the tip-sample distance, respectively. In both results, as the tip-sample distance was decreased, the magnitude of both components increased due to the increase in C_B. The purple broken line shows the offset caused by the electrostatic force acting on the cantilever, which has almost no dependence on the tip-sample distance. The increase in the $2\omega_m$ component was almost double the offset at the closest distance, while the ω_m component showed a steep increase. The blue and green broken curves shown in Fig. 4.5b, c are the fitting curves calculated by the theoretical equation, (4.24), without and with taking into account the voltage division by C_S in (4.27), respectively. From the best fitted parameters, the local surface potential difference under the CP was estimated to be 0.25 V. We also obtained the parameters such as $L_D = 30$ nm and $C_S = 0.011$ F/m^2 by the fitting. L_D was shorter than that expected from (4.8) probably because of the dissolved CO_2 from the ambient, while C_S was smaller than the literature value of 0.2–0.3 F/m^2 [15] probably because of the surface roughness, adsorbates or contaminants.

Finally, we discuss the criteria for the geometry of the cantilever and tip required for the local surface potential measurements. Reduction of the cantilever dimensions and increase of the tip height both would lead to the reduction of the parasitic long-range electrostatic force. In particular, the reduction of the cantilever dimensions is preferred because it increases the resonance frequency, which is favorable for sensitive force detection. Note that even if such a dedicated force sensor is available, the Stern layer capacitance and the dielectric constant that is typically lower than the liquid media attenuate the voltage division ratio in the bulk solution and thereby attenuate the local electrostatic force. Therefore, great care should be taken to estimate the local surface potential using the voltage modulation techniques.

4.5 Surface Charge Measurement by Force Mapping

We have shown that the detection of the capacitive and electrostatic force induced by the modulation voltage application are fairly complicated. It is rather straightforward to directly measure the electrostatic force acting on the cantilever with a tip as a function of the tip-sample distance by a force distance curve measurement, and then analyze it to deduce the surface charge and/or surface potential [16–20]. In this section, we demonstrate the local charge density measurement of plasmid DNA molecules using frequency modulation AFM (FM-AFM). For small-amplitude FM-AFM, the frequency shift (Δf) signal is approximately proportional to the force gradient. Hence, an increase in the electrolyte concentration leads to an increase in the observed Δf signal as well as in the spatial resolution because of the decrease in L_D despite the weakening of the F_{el} itself.

We used plasmid pUC18 (2686 base pairs) DNA molecules (Takara Bio) on a muscovite mica (Furuuchi Chemical) as a model sample. We coated the mica substrate with a positively charged poly-L-lysine (PL) layer. A water solution of the DNA (2–3 mg/L) was dropped onto the PL-coated mica surface. After 5–10 min, the sample was rinsed with a KCl solution, and imaged by FM-AFM without drying.

We used a home-built FM-AFM setup with an ultra-low noise deflection sensor [21] and a photothermal excitation setup [22]. We used a cantilever with a spring constant of about 30 N/m. The resonance frequency of the cantilever in the solution was about 150 kHz. The oscillation amplitude was set to 0.4 and 0.8 nm peak-to-peak in the 100 mM and 10 mM KCl solutions which were slightly smaller than L_D (0.97 and 3.07 nm at 298 K), respectively, to obtain a better spatial resolution. We obtained 3D Δf maps in a volume of $60 \times 40 \times 8.8$ nm^3 ($128 \times 64 \times 200$ pixels) in XYZ by consecutively collecting Δf maps in 2D(ZX) planes, which were collected by recording the Δf data while approaching the tip to the sample surface with a velocity of about 300 nm/s (corresponding to a triangular waveform of about 17 Hz) until Δf reached a predetermined threshold value [23].

For calculation of the surface charge from the measured frequency shift map, we employed the DLVO (Derjaguin, Landau, Verwey and Overbeek) force model [24], which assumes the total interaction force as the sum of F_{el} and van der Waals force (F_{vdW}). For a 1:1 symmetric electrolyte, the EDL force vector acting between two surfaces is calculated by

$$\overrightarrow{\mathbf{F}}_{el} = \iint_S \left\{ 2n^{\infty} k_B T \left[\cosh\left(\frac{e\phi}{k_B T} \right) - 1 \right] \mathbf{I} - \frac{\varepsilon_r \varepsilon_0}{2} (\nabla \phi)^2 \right\} \cdot \hat{\mathbf{n}} \, dS, \tag{4.28}$$

where the z component of $\overrightarrow{\mathbf{F}}_{el}$ gives F_{el}. The first term is the osmotic pressure tensor term, which is always repulsive, and the second term is the Maxwell stress tensor term, which is always attractive, both of which can be calculated once the distribution of the potential is determined [25, 26]. $\mathbf{I}$ and $\hat{\mathbf{n}}$ are the unit tensor and

the unit normal vector, respectively. We calculated the potential distribution by solving the Poisson-Boltzmann equation [27, 28]. While the constant charge or constant potential condition is commonly known, the surface conditions in the electrolytes are always somewhere between these extremes (charge regulation) [11, 29]. We calculated the potential distribution with the LSA [13, 30]. Namely, we first calculated the surface potential and charge densities of the two surfaces under the condition that the EDLs do not overlap. Secondly, the potential distribution between the two surfaces was determined by linearly superposing the effective potential distributions calculated for the two surfaces using the potential formulae. Finally, F_{el} acting between the surfaces was calculated using (4.28) from the potential and the electric field [24, 30]. Then we calculated the theoretical Δf_{el} curves from the theoretical F_{el} curves using the experimental parameters. The DNA molecule was modeled as a cylinder with a radius of 1.3 nm considering the hydration layers on the DNA, and the tip radius was set to 12 nm as it gave the best fit of the theoretical Δf curves to the experimental Δf curves.

For calculation of F_{vdW}, we employed the surface element integration (SEI) method using the Derjaguin construction [25], as

$$F_{vdW}(z+z_0) = \iiint_{V_t} \iiint_{V_s} F_{atom-atom}(r)\mathrm{d}V_s\mathrm{d}V_t \approx \iint_{S_{ts}} P_{vdW}\,\mathrm{d}S_{ts}, \tag{4.29}$$

where z_0 is an offset parameter used to correct the difference in the onset position of the F_{vdW}. P_{vdW} is F_{vdW} per unit area given by

$$P_{vdW}(z) = -\left[A_H^{\nu=0}\exp(-2z/\lambda_D) + A_H^{\nu>0}\right]\frac{1}{6\pi z^3}, \tag{4.30}$$

where $A_H^{\nu=0}$ and $A_H^{\nu>0}$ are the Hamaker constants representing the zero-frequency and dispersion contributions, respectively. The radius of the DNA was set to 1.0 nm for the calculation of F_{vdW}.

Figure 4.6a, b show the topography images reconstructed from the 3D Δf maps. The helical structures of the DNA molecules are visible in both images, as indicated by the arrows in the images. The helical structures are less clear than our previous result [31] mainly due to the larger roughness of the PL layer surface. Figure 4.6c, d show the 2D(XY) Δf maps obtained at a distance of around 0.4 nm above the DNA molecules in the 100 mM and 10 mM solutions, respectively. Figure 4.6e, f show the 2D(ZX) Δf maps obtained in the XY planes including lines A–B and C–D that cross the DNA molecules in the 100 mM and 10 mM solutions, respectively. The yellow pixels in each map represent the points without data because the tip was retracted. The interface of the regions with and without data in each map represents the topographic line profile, from which the heights of the DNA molecules are estimated to be about 1.8 and 1.6 nm in the 100 mM and 10 mM solutions, respectively.

In principle, repulsive and attractive F_{el} are expected on the DNA molecules and the PL layer, respectively. Since L_D is half the height of the DNA molecules in the

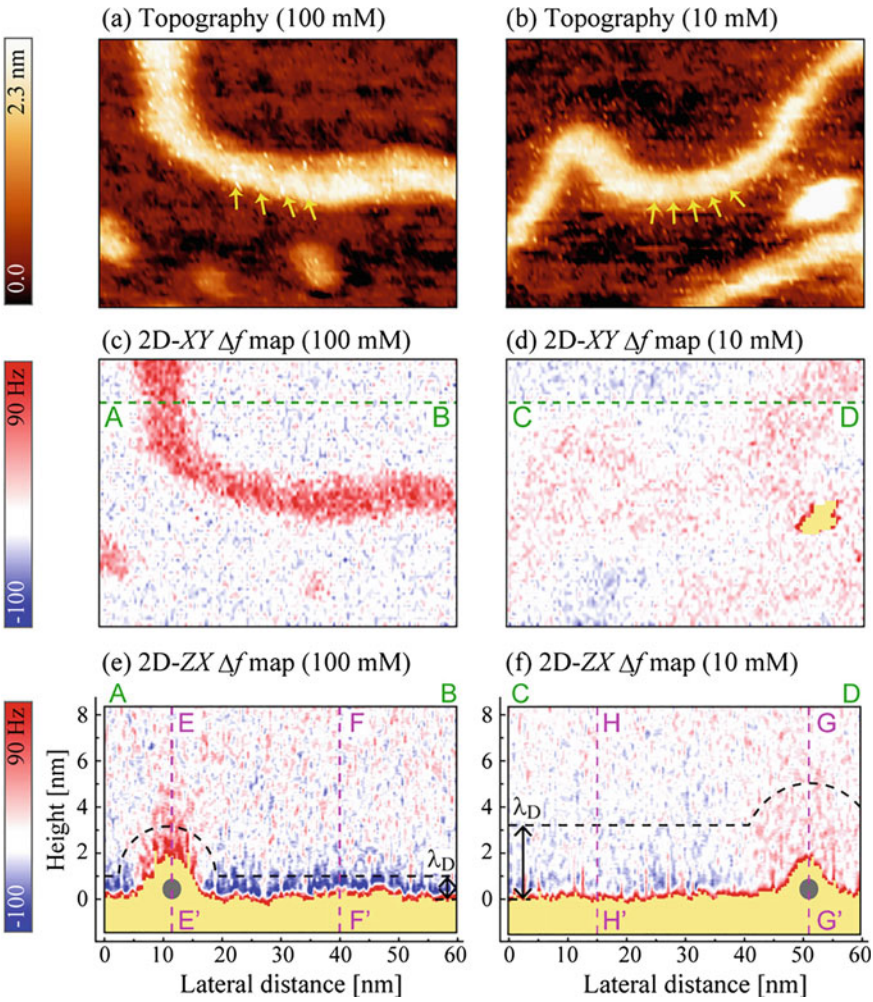

Fig. 4.6 **a** and **b** are topography images of plasmid DNA molecules on mica coated with a poly-L-lysine layer at constant Δf of +100 Hz reconstructed from 3D Δf data in 100 mM and 10 mM KCl solutions, respectively. The arrows indicate the helical periodicity of the DNA molecules, which is about 3.6 nm. **c** and **d** are 2D(XY) Δf maps obtained at the surface of 0.4 nm from DNA in 100 mM and 10 mM KCl solutions, respectively. **e** and **f** are 2D(ZX) Δf maps of the plasmid DNA molecules extracted from the 3D Δf data in a ZX plane crossing DNA in 100 mM and 10 mM KCl solutions, respectively. The black dotted curves schematically indicate L_D in each solution. Reprinted from [19], © IOP Publishing. Reproduced with permission. All rights reserved

100 mM KCl solution, the EDL of the PL layer (blue area) is not overlapped with that of the DNA molecule (red area). On the other hand, in the 10 mM KCl solution, L_D is 1.5 times larger than the height of the DNA molecule. Hence the EDL of the PL substrate (blue) is overlapped with that of the DNA molecule (red).

Therefore, F_{el} on the DNA molecule is not solely reflected by the EDL of the DNA molecule, but also reflected by the EDL on the PL layer in 10 mM solution.

We then constructed theoretical 2D Δf_{el} maps to determine if they are consistent with the experimental 2D(XY) Δf_{el} maps. Figure 4.7a, b show the theoretical 2D Δf_{el} maps for 100 mM and 10 mM KCl solutions, respectively. The lateral size of the DNA molecule was set to about 7 times larger than the actual size considering the tip convolution effect. Note that Δf_{el} caused by F_{el} spreads out to the distance of L_D in each map.

Figure 4.7c shows the averaged Δf versus distance curves measured on the DNA molecule and the PL layer in the 100 mM solution at the locations indicated by the E–E′ and F–F′ lines, respectively, in Fig. 4.6e. The red and blue solid curves are obtained on the DNA molecule and PL layer, respectively. On both surfaces, the exponential F_{el} is dominant at distances larger than 0.5 nm, while F_{vdW} and Pauli repulsion force are dominant at distances less than 0.5 nm. Since Fig. 4.6e showed that the EDL of the PL substrate (blue area) was not overlapped with that of the

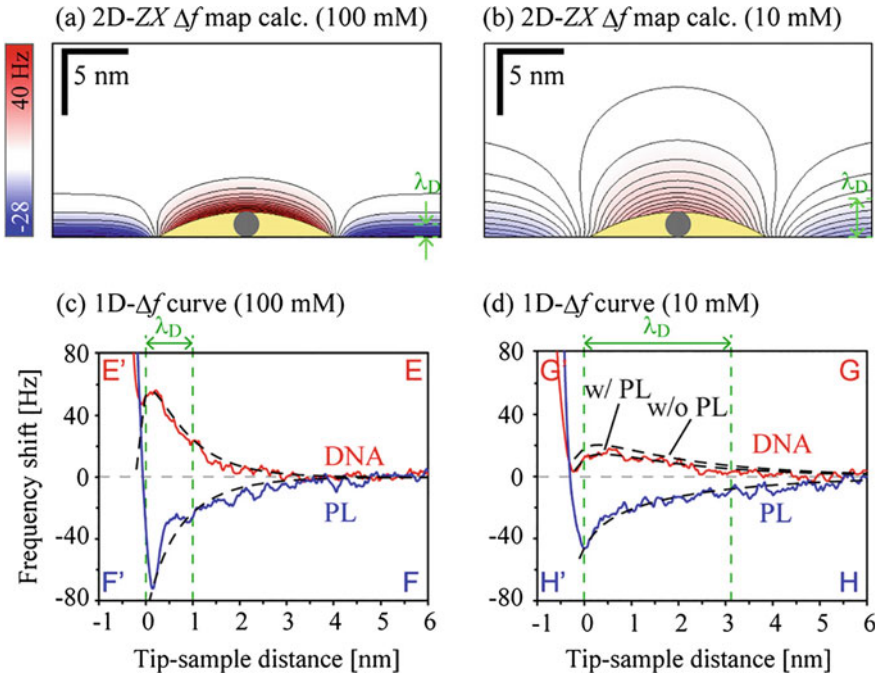

Fig. 4.7 **a** and **b** are theoretically calculated 2D(ZX) Δf_{el} maps (30 × 15 nm^2) in 100 mM and 10 mM KCl solutions, respectively. The gray circles indicate the positions of the DNA molecules. **c** and **d** are 1D Δf curves extracted from the 2D(ZX) Δf maps in 100 mM and 10 mM KCl solutions. The red and blue curves show the experimental data obtained on the DNA molecules and the PL substrate, respectively, and the black dotted curves show the theoretical curves that gave the best fit. Reprinted from [19], © IOP Publishing. Reproduced with permission. All rights reserved

DNA molecule (red area) in the 100 mM solution, we calculated the theoretical force curve on the DNA molecule by setting n^{∞} = 130 mM and pH = 6.0 of the solutions as the fitting parameters. Note that the PL layer was not taken into account in this case, and we set the charge density of the DNA (σ_{DNA}) as −150 mC/m^2. The theoretical Δf_{el} curve that gave the best fit to the experimental Δf curve on the DNA is shown as the dotted curve in Fig. 4.7c. For these conditions ϕ_{silica} and σ_{silica} were determined to be −6 mV and −17 mC/m^2, respectively. This result suggests that the charge density of the molecule can be quantitatively evaluated using FM-AFM in a strong electrolyte.

In the case of the 10 mM solution, we found from Fig. 4.6f that the EDL of the PL substrate (blue area) was overlapped with that of the DNA molecule (red area). In such a case, the PL substrate should be taken into account to estimate the charge density on the DNA molecule because F_{el} measured on the DNA molecule was influenced by the positive charges on the PL substrate. We plotted the theoretical Δf_{el} curves on the DNA molecule that gave the best fit to the experimental Δf curve using the models with and without the PL layer in the 10 mM solution in Fig. 4.7d, using the parameters n^{∞} = 15 mM and pH = 5.7. We found that the theoretical Δf_{el} for the model with the PL layer was about 30% larger than that calculated for the model without the PL layer. The result suggests that it is difficult to estimate the charge density in an electrolyte of such a low concentration with a nanometer-scale resolution. Therefore, the charge density measurement by FM-AFM in a strong electrolyte is preferred.

4.6 Summary

This chapter reviews the practical aspects of the surface potential and charge measurement based on the electrostatic force detection in liquid environment. We first reviewed the basic properties of the EDL, and then analyzed the capacitive force and electrostatic force induced by the alternating modulation voltage. We presented the criteria for the modulation frequency for obtaining high spatial resolution in local surface charge and potential measurements, namely $f_m > f_D$ and $f_m > f_c$. Several researchers have also demonstrated the electrostatic force detection based on the voltage modulation technique with a modulation frequency that meets the criteria [5, 32–35].

We observed a long-range parasitic electrostatic force even when a high-frequency modulation voltage that meets the criteria was used, and suggested the use of a cantilever with a small surface area and/or a tip with a high aspect ratio. We then demonstrated a local surface potential and charge measurement using a CP cantilever. Even if the local information on the surface charge or surface potential under the tip can be detected, the KPFM bias feedback may not be used since the dependence of the electrostatic force on the applied dc voltage was not straightforward.

Finally, we also demonstrated a surface charge measurement on a biological sample using the 3D force mapping technique, which is an alternative method to map the local surface charge and potential in liquid media. Since the lateral resolution is determined by the overlap of the EDLs, the charge density measurement with a nanometer-scale resolution is only feasible in a strong electrolyte.

References

1. A.J. Bard, L.R. Faulkner, *Electrochemical Methods, Fundamentals and Applications,* 2nd edn. (Wiley, 2001)
2. K. Umeda, K. Kobayashi, N. Oyabu, Y. Hirata, K. Matsushige, H. Yamada, J. Appl. Phys. **113**, 154311 (2013)
3. T.L. Sounart, T.A. Michalske, K.R. Zavadil, J. Microelectromech. Syst. **14**, 125 (2005)
4. V. Mukundan, P. Ponce, H.E. Butterfield, B.L. Pruitt, J. Micromech. Microeng. **19**, 065008 (2009)
5. L. Collins, S. Jesse, J.I. Kilpatrick, A. Tselev, O. Varenyk, M.B. Okatan, S.A.L. Weber, A. Kumar, N. Balke, S.V. Kalinin, B.J. Rodriguez, Nat. Commun. **5**, 3871 (2014)
6. S. Hudlet, M. Saint Jean, C. Guthmann, J. Berger, Eur. Phys. J. B **2**, 5 (1998)
7. J. Colchero, A. Gil, A.M. Baró, Phys. Rev. B **64**, 245403 (2001)
8. F. Booth, J. Chem. Phys. **19**, 391 (1951)
9. L. Yang, B.H. Fishbine, A. Migliori, L.R. Pratt, J. Chem. Phys. **132**, 044701 (2010)
10. D.Y.C. Chan, D.J. Mitchell, J. Colloid Interface Sci. **95**, 193 (1983)
11. R. Pericet-Camara, G. Papastavrou, S.H. Behrens, M. Borkovec, J. Phys. Chem. B **108**, 19467 (2004)
12. R. Hogg, T.W. Healy, D.W. Fuersten, Trans. Faraday Soc. **62**, 1638 (1966)
13. H. Ohshima, *Biophysical Chemistry of Biointerfaces*. (Wiley, 2010)
14. K. Umeda, K. Kobayashi, N. Oyabu, Y. Hirata, K. Matsushige, H. Yamada, J. Appl. Phys. **116**, 134307 (2014)
15. D.C. Grahame, Chem. Rev. **41**, 441 (1947)
16. J. Sotres, A.M. Baró, Appl. Phys. Lett. **93**, 103903 (2008)
17. J. Sotres, A.M. Baró, Biophys. J. **98**, 1995 (2010)
18. I. Siretanu, D. Ebeling, M.P. Andersson, S.L.S. Stipp, A. Philipse, M.C. Stuart, D. van den Ende, F. Mugele, Sci. Rep. **4**, 4956 (2014)
19. K. Umeda, K. Kobayashi, N. Oyabu, K. Matsushige, H. Yamada, Nanotechnology **26**, 285103 (2015)
20. C. Zhao, D. Ebeling, I. Siretanu, D. van den Ende, F. Mugele, Nanoscale **7**, 16298 (2015)
21. T. Fukuma, M. Kimura, K. Kobayashi, K. Matsushige, H. Yamada, Rev. Sci. Instrum. **76**, 053704 (2005)
22. K. Kobayashi, H. Yamada, K. Matsushige, Rev. Sci. Instrum. **82**, 033702 (2011)
23. K. Kobayashi, N. Oyabu, K. Kimura, S. Ido, K. Suzuki, T. Imai, K. Tagami, M. Tsukada, H. Yamada, J. Chem. Phys. **138**, 184704 (2013)
24. J.N. Israelachvili, *Intermolecular and Surface Forces*, 3rd edn. (Academic Press, 2010)
25. S. Bhattacharjee, M. Elimelech, J. Colloid Interface Sci. **193**, 273 (1997)
26. V.A. Parsegian, D. Gingell, Biophys. J. **12**, 1192 (1972)
27. D.Y.C. Chan, R.M. Pashley, L.R. White, J. Colloid Interface Sci. **77**, 283 (1980)
28. D. McCormack, S.L. Carnie, D.Y.C. Chan, J. Colloid Interface Sci. **169**, 177 (1995)
29. I. Popa, P. Sinha, M. Finessi, P. Maroni, G. Papastavrou, M. Borkovec, Phys. Rev. Lett. **104**, 228301 (2010)
30. S. Lin, M.R. Wiesner, Langmuir **26**, 16638 (2010)

31. S. Ido, K. Kimura, N. Oyabu, K. Kobayashi, M. Tsukada, K. Matsushige, H. Yamada, ACS Nano **7**, 1817 (2013)
32. N. Kobayashi, H. Asakawa, T. Fukuma, Rev. Sci. Instrum. **81**, 123705 (2010)
33. N. Kobayashi, H. Asakawa, T. Fukuma, Rev. Sci. Instrum. **83**, 033709 (2012)
34. K. Honbo, S. Ogata, T. Kitagawa, T. Okamoto, N. Kobayashi, I. Sugimoto, S. Shima, A. Fukunaga, C. Takatoh, T. Fukuma, ACS Nano **10**, 2575 (2016)
35. L. Collins, S. Jesse, J.I. Kilpatrick, A. Tselev, M.B. Okatan, S.V. Kalinin, B.J. Rodriguez, Beilstein J. Nanotechnol. **6**, 201 (2015)